Graphical Abstract

Influence of incoming turbulence on aerodynamic forces of a high-speed train

Huanxia Wei, Chao Xia, Qing Jia, Simone Sebben, Zhigang Yang

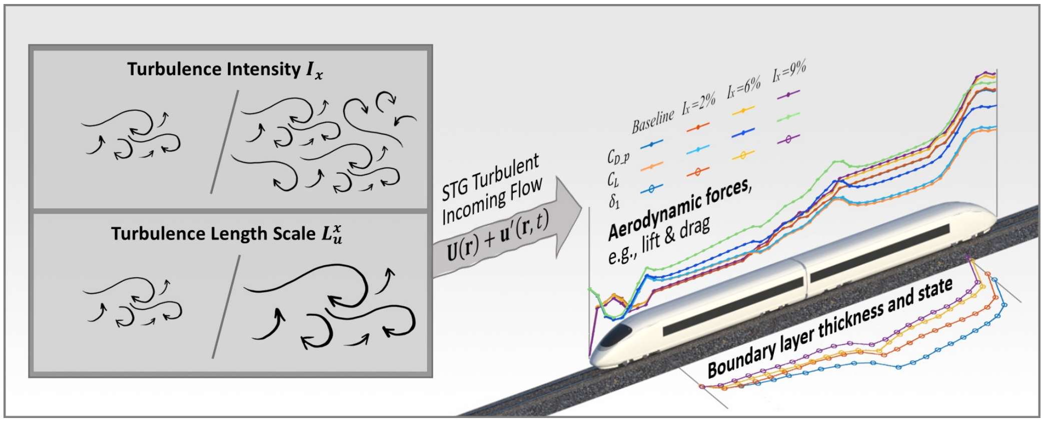

Highlights

Influence of incoming turbulence on aerodynamic forces of a high-speed train

Huanxia Wei, Chao Xia, Qing Jia, Simone Sebben, Zhigang Yang

- Numerical simulation of high-speed trains under turbulence conditions is conducted using IDDES and STG methods.
- Both drag and lift forces increase with higher turbulence intensity.
- The influence of turbulence length scale is considered for the first time, revealing that larger incoming turbulence length scales lead to greater drag and lift forces on high-speed trains.
- The underlying mechanisms of these changes are elucidated by analyzing the flow topology in various key regions.

Influence of incoming turbulence on aerodynamic forces of a high-speed train

Huanxia Wei[a], Chao Xia[a,b,*], Qing Jia[a], Simone Sebben[b], Zhigang Yang[a,c]

[a]*School of Automotive Studies, Tongji University, Shanghai, 201804, China*
[b]*Department of Mechanics and Maritime Sciences, Chalmers University of Technology, Gothenburg, 412 96, Sweden*
[c]*Beijing Aeronautical Science and Technology Research Institute, Beijing, 102211, China*

Abstract

The influence of incoming turbulence on the aerodynamics of a high-speed train is numerically investigated using the Improved Delayed Detached Eddy Simulation (IDDES) combined with Synthetic Turbulence Generation (STG). The results reveal that increasing turbulence intensity significantly enhances the drag and lift coefficients of the train, with the rate of increase amplifying as the turbulence length scale grows. The incoming turbulence induces effects analogous to crosswind conditions, weakening the aerodynamic impact on the head carriage while accelerating airflow around the curved sections of the tail carriage. Moreover, the turbulent kinetic energy within the shear layers adjacent to the bogie cavity increases with turbulence intensity, facilitating enhanced flow ingress into the cavity and intensifying interactions with the bogie and cavity structures, thereby augmenting both drag and lift. Additionally, the presence of incoming turbulence produces a thinner boundary layer, characterized by a reduced shape factor and elevated viscous drag. Specifically, higher turbulence intensity leads to a smaller shape factor and a steeper velocity gradient, thereby increasing viscous drag. In contrast, larger turbulence length scales exhibit the opposite trend, manifesting as a decrease in viscous drag.

Keywords: Train aerodynamics, Incoming turbulence, Synthetic turbulence generation, Aerodynamic force, Boundary layer

*Corresponding author.
Email address: chao.xia@tongji.edu.cn (Chao Xia)

1. Introduction

Research methods for aerodynamics of a high-speed train (HST) include wind tunnel tests [1, 2], moving model experiments [3, 4], numerical simulations [5, 6, 7], etc. In these present studies, the inlet conditions are characterized by low turbulence or laminar flow. However, influenced by factors such as natural winds, trackside equipment, embankments, tunnels, and viaducts, the actual wind encountered on train routes is highly non-uniform. Yu et al. modeled the turbulent incoming flow conditions due to natural wind during the operation of HSTs, and the turbulence intensity was calculated as about 24.5% at the measurement point from EN 14067-6 locating at $h = 4.0m$ [8]. Wordley et al. found that turbulence intensity of real conditions for ground vehicles ranges from 2% to 16%, or even higher, with a turbulence length scale ranging from 1 to 20 meters [9]. Gao proposed that turbulent incoming flow and crosswinds significantly affect the safety and economy of HSTs [10]. The accuracy and reliability of aerodynamic characteristics obtained from numerical simulations or wind tunnel experiments can be significantly influenced by inlet flow conditions that deviate from real-world environments. Consequently, it is essential to investigate the effects of incoming turbulence on the aerodynamic performance of HSTs to enhance the relevance and applicability of research findings to actual operational conditions.

In the majority of research papers examining the impact of turbulence, the desired turbulence components are typically introduced at the inlet through experimental methods, with the research focus primarily on basic geometry models. These models include square prisms [11, 12, 13, 14], Ahmed bodies [15], and simplified vehicle models [16]. The turbulence generation devices utilized to introduce turbulence components include passive turbulence grids [11, 12, 13, 14], active grids [17], spires [16], swing mechanisms [18, 19], and specialized systems [20, 21]. In addition to wind tunnel testing, recent studies have utilized numerical simulations in combination with synthetic turbulence generation (STG) methods to investigate the effects of turbulence [22, 23, 24], as numerical methods provide improved efficiency in generating the desired turbulence intensity and length scales, as well as more convenient result measurement.

In recent years, numerous studies have investigated the impact of turbulence on ground vehicles. FKFS built the turbulence generation system "FKFS Swing" in both full-scale and 1/4 scaled automotive wind tunnels with the purpose of reconstructing road turbulence conditions in tests

[18, 25], and later proposed a correction method for turbulent wind tunnel testing, decoupling the influence of the unsteady flow from that of the static pressure gradient in the wind tunnel [26, 19]. Based on this, they measured the aerodynamic drag on various vehicle models under turbulent conditions, and concluded that higher turbulence intensity increases drag. Furthermore, this effect varies significantly depending on the vehicle design, highlighting the importance of considering unsteady incoming conditions [27]. Cogotti et al. observed that an increase in the turbulence intensity leads to a significant increase in both the drag and the lift forces on a car in a wind tunnel, with the lift increasing by 120 counts and the drag by 20-30 counts. McAuliffe et al. developed the Road Turbulence System (RTS) in the 9 m NRC wind tunnel with the aim of reconstructing turbulent road wind conditions in experiments [21], and proved its performance compared to various other passive and active turbulence generation devices [20]. This approach was used to study the drag characteristics of a heavy duty vehicle (HDV) and a standard SUV, revealing that the positive-drag area of HDV is larger in uniform incoming flow, contrarily, that of SUV in turbulent incoming flow is larger. Gaylard et al. applied the unsteady Lattice-Boltzmann method (LBM) to simulate 4% and 7% turbulence intensity conditions by superimposing a three-dimensional unsteady velocity field onto uniform conditions, examining the influence of turbulence on a fastback saloon model. The results indicated that both drag and lift increased under turbulent conditions [28]. Duncan et al. also used LBM to explore the impact of turbulence on an SUV, a squareback vehicle, and a notchback vehicle, demonstrating that the drag of all three models increased under turbulent conditions, accompanied by changes in the shear layer and wake structures, suggesting a non-linear relationship between turbulence and its effects on vehicles [29].

However, due to the complicated geometry of HSTs, only limited investigations have explored the effects of turbulence and non-uniform wind on their aerodynamic characteristics. Common approaches involve introducing spires at the entrance of the wind tunnel, with a focus on crosswind influences [30, 31, 32, 33, 34]. Robinson et al. conducted experiments on a 1/50 scaled train model in a wind tunnel to assess the impact of turbulence [35]. Their results revealed that side force coefficients, lift force coefficients, and vortex core distributions were influenced by the interaction between vortical structures and the train wake, thereby affecting force and moment coefficients. Bocciolone et al. demonstrated that turbulence has a pronounced influence on aerodynamic coefficients through comprehensive wind tunnel testing, especially at high attack angles [31]. Consistently, Cheli et al. showed that aerodynamic forces increase with turbulence intensity [32]. However, Niu et al. reported contrasting findings, observing that higher turbulence intensity led to drag reduction and a decrease in surface pressure on both the head and tail carriages of HST [36]. Xue et al. numerically investigated the influence of turbulent incoming flow on an HST with a yaw angle of 90 ° based on IDDES, interestingly, they found that when the turbulence length scale is greater than a crisis threshold of $0.5H$, load fluctuations are reduced [37], and later expanded their study to wider yaw angles under turbulence intensities of 5% and 20% [38]. Garca et al. conducted numerical simulations with WMLES on HST under synthetic crosswind based on the Kaimal spectrum in TurbSim with both smooth and rough train surfaces, and compared the results of aerodynamic forces and moments [39], and then they compared the results under steady wind and turbulent winds generated by Kaimal spectrum (TurbSim) and Smirnov method (Ansys Fluent) [22]. Gao et al. investigated the turbulence correlation between moving trains and anemometer towers, mainly focusing on the stability under crosswind [10]. Deng et al. reconstructed the structural wind when the HST running through a tunnel-flat ground-tunnel scenario in the wind tunnel tests with spire and the fence, and in numerical studies with IDDES as well [40, 41]. Yang et al. compared the turbulent wind characteristics over tunnel-bridge (TB) and tunnel-flat ground (TF) infrastructures for a passing HST, and proposed that the TB sites have a lower turbulence intensity about 8% due to elevated and unobstructed locations rather than TF sites, which has a higher turbulence intensity about 10% according to near-ground effect [42].

In summary, current research on the impact of turbulence on HSTs has primarily focused on aerodynamic forces. Due to the lack of detailed flow field data and pressure distribution information, the mechanism through which turbulence affects aerodynamics remains unclear, and conclusions are inconsistent. Furthermore, previous studies have largely overlooked the effects of turbulence length scales. The primary objective of this paper is to address these gaps by investigating the influence of both turbulence intensity and turbulence length scales on the aerodynamic characteristics of HSTs. In addition to aerodynamic forces, flow field details such as surface pressure distribution, flow around the bogie cavities, and boundary layer formation and development are analyzed to provide deeper insights into the underlying mechanisms.

The remainder of this paper is structured as follows. Section 2 introduces the setup of the numerical simulation cases, including the geometric models, numerical methods, as well as the initial and boundary conditions. Additionally, the methods for synthetic turbulence generation and turbulence representations are briefly described. Section 3 focuses on the impact of varying turbulence intensity and length scale on aerodynamic forces, boundary layer characteristics, and surface pressure distributions, providing a detailed discussion of the underlying mechanisms and the potential link between them. Finally, the conclusions are summarized in Section 4.

2. Methods

2.1. Geometry and computational domain

A 1/18 scaled CRH3 HST model with two carriages is used in the simulation (Figure 1). The model measures 2.894 m in length (L) × 0.183 m in width (W) × 0.201 m in height (H). In addition to four bogies and bogie cavities, two cowcatchers and one intercarriage junction gap (hereinafter referred to as "carriage junction") are also included.

As shown in Figure 2, the dimensions of the computational domain are 64.4H × 25H × 20H (length × width × height), where H represents the height of the HST model. In the underbody region of the HST, a 1/18 single track ballast and rail (STBR) ground configuration is implemented, in accordance with the Technical Specifications for Interoperability (TSI) standard [43]. The boundary conditions are set as follows: a velocity inlet and pressure outlet, a non-slip wall condition for the train body, a slip wall with a matching the inlet velocity for the STBR and ground, and slip walls for the others boundaries. The free stream velocity U_∞ is 58 m/s, resulting in a Reynolds number of 7.2×10^5, based on U_∞ and the carriage width W.

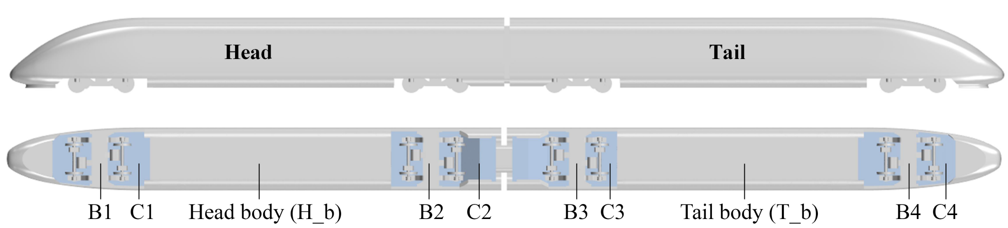

Figure 1: Geometry of 1/18 scaled CRH3 HST model. C represents the bogie cavity, and B represents the bogie. H_b and T_b are head body and tail body, respectively. These abbreviations are to be referred hereunder.

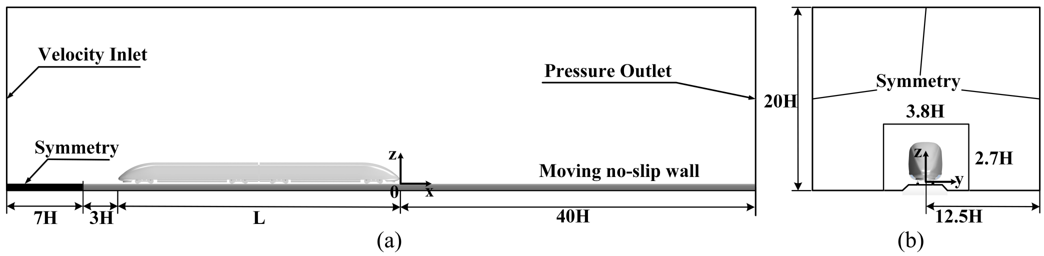

Figure 2: Computational domain and boundary conditions. The coordinate system (x, y, z) is superposed, with the origin located at the top of the rail. The small rectangle with width of 3.8H in (b) indicates the STG region.

To investigate the influence of incoming turbulence, various turbulence intensities and length scales are introduced at the inlet using synthetic turbulence generation (STG)[23], which is applied in the region where the mesh size is relatively uniform, as indicated by the small rectangle in Figure 2b.

2.2. Numerical method

The improved delayed detached eddy simulation (IDDES), based on $k-\omega$ SST, is employed for the numerical study. Proposed by Shur et al.[44], IDDES combines the advantages of delayed detached eddy simulation (DDES) and wall-modeled large eddy simulation (WMLES), and will activate RANS and LES in different regions to obtain a satisfactory balance between computational accuracy and computational resource consumption. In our previous studies, the same model was used, with detailed descriptions of the numerical method provided in [5, 45, 46].

In this study, to achieve satisfactory reliability and numerical accuracy, the domain is discretized using Poly-Hexcore mesh, which automatically connects the prism layers to the hexahedral mesh regions. Three mesh sets with different refinement levels (coarse, medium, and fine) are used in the convergence check to demonstrate mesh independence, consisting of 23.3, 38.5, and 50.6 million cells, respectively. The primary differences among these grids lie in the spatial resolution on the surface and in the wake region, as listed in Table 1. The near-wall boundary layers for them remain consistent, each containing 20 extruded cells with $y^+ \leq 1$ and a total height of 0.03H. The mesh at the medium refinement level around the train with details is shown in Figure 3.

Table 1: Spatial resolution details for mesh of the train, bogie, and wake region.

Refinement level	**Train surface**	**Bogie surface**	**Wake region**	**Total mesh number**
Coarse	0.01 - 0.03 H	0.01 - 0.015 H	0.03 H	23.3 million
Medium	0.005 - 0.02 H	0.005 - 0.01 H	0.02 H	38.5 million
Fine	0.005 - 0.015 H	0.005 - 0.01 H	0.018 H	50.6 million

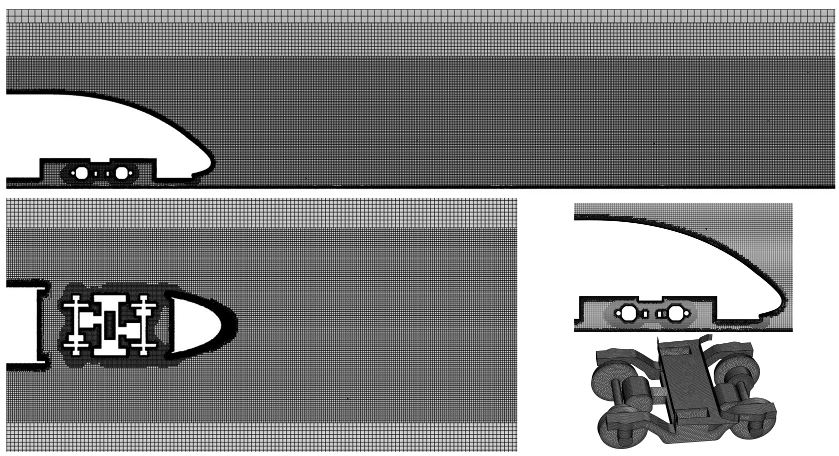

Figure 3: Mesh distribution around a HST at medium refinement level.

2.3. Mesh convergence and numerical validation

To ensure the numerical reliability of the simulations, a series of mesh convergence check was conducted to verify the mesh independence. Subsequently, the numerical results were validated against the wind tunnel data to confirm their accuracy.

For the mesh convergence study, force coefficients are treated as convergence criteria, and defined by Eq. 1-3, where C_D, C_{Dp}, C_{Dv}, C_L and C_S are the drag coefficient, pressure drag coefficient, viscous drag coefficient, lift coefficient, and side force coefficient, respectively.

$$C_D = \frac{F_x}{\frac{1}{2}\rho U_\infty^2 A_x}, C_{Dp} = \frac{F_{xp}}{\frac{1}{2}\rho U_\infty^2 A_x}, C_{Dv} = \frac{F_{xv}}{\frac{1}{2}\rho U_\infty^2 A_x} \tag{1}$$

$$C_L = \frac{F_z}{\frac{1}{2}\rho U_\infty^2 A_x} \tag{2}$$

$$C_S = \frac{F_y}{\frac{1}{2}\rho U_\infty^2 A_x} \tag{3}$$

where F_x, F_{xp}, F_{xv}, F_y and F_z are the total drag, pressure drag, viscous drag, side force and lift force, respectively. Additionally, ρ is the density of the air, U_∞ is the free stream velocity, and A_x is the projected area in the streamwise direction. The pressure coefficient C_P is defined in Eq. 4, where P is the time-averaged surface pressure and P_∞ is the static pressure of the incoming flow.

$$C_P = \frac{P - P_\infty}{\frac{1}{2}\rho U_\infty^2} \tag{4}$$

For numerical validation, the simulation under stationary ground conditions for the train with three carriages is compared against the wind tunnel tests conducted at the Shanghai Automotive Wind Tunnel Center (SAWTC). This validation includes aerodynamic forces and pressure measurements. The Reynolds number for the wind tunnel test is 7.20×10^5, consistent with the numerical simulation. The HST model used in the wind tunnel test is at a 1/8 scale and retains the detailed crescent-shaped structures and air conditioning fairings, which are simplified in the numerical simulation. More detailed information regarding the wind tunnel tests was provided in our previous study [45].

Figure 4a shows the time-averaged C_D for the head carriage, tail carriage, and the entire train set across the three refinement levels, alongside the wind tunnel tests. The numerical results for all cases show good agreement. For the three different mesh refinement levels, the deviation in C_D among the

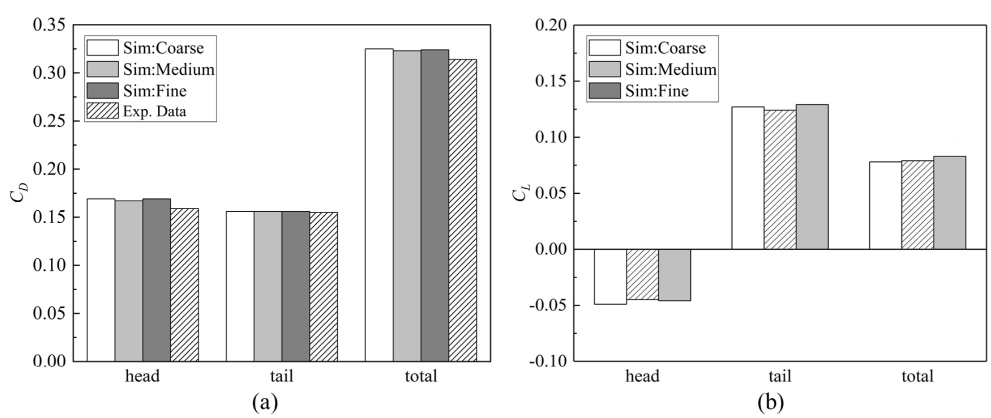

Figure 4: Time-averaged force coefficients of the head carriage, tail carriage and total train set based on coarse, medium and fine mesh and wind tunnel tests: (a) C_D and (b) C_L.

meshes is less than 1%. Compared with the wind tunnel data, the deviation in C_D for both head and tail carriage in the IDDES (medium refinement) is less than 5%. For C_L (Figure 4b), the deviation among the three meshes is less than 7%, and between the medium and fine mesh is within 4%.

Figure 5 presents the distribution of C_P along the longitudinal symmetry line of the upper surface for the head and tail carriages, comparing the numerical results from three meshes levels with the wind tunnel tests. For the mesh convergence, the results for the three refinement levels are generally in good agreement,with minor discrepancies observed for the coarse mesh, particularly at the nose edge of the tail carriage. The pressure distribution from the IDDES with medium refinement level also demonstrates good agreement with the experimental results.

Overall, considering the balance between computational cost and accuracy, subsequent simulations are conducted using the medium mesh. The results from this mesh show satisfactory mesh independence and are well-aligned with the wind tunnel data in terms of aerodynamic forces and pressure distribution.

2.4. Turbulence representations and generation

Turbulence measures focused in this study include turbulence intensity and turbulence length scale. Turbulence intensity is an critical parameter to represent the level of turbulence in the wind, defined as the ratio of velocity fluctuations to the mean velocity [47]. Accordingly, the turbulence intensity

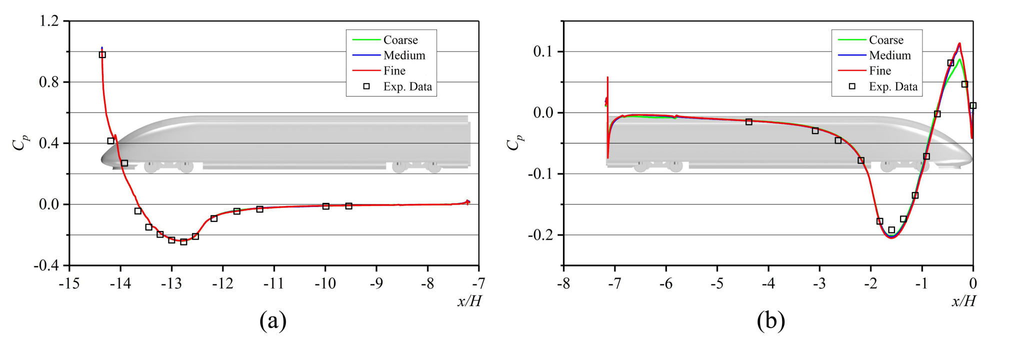

Figure 5: Time-averaged C_P of the longitudinal symmetry line based on coarse, medium and fine mesh and wind tunnel tests: (a) the head carriage; (b) the tail carriage.

in three directions is expressed as follows:

$$I_x = \frac{U_{rms}}{U_\infty}, \quad I_y = \frac{V_{rms}}{U_\infty}, \quad I_z = \frac{W_{rms}}{U_\infty}, \tag{5}$$

where I_x, I_y, and I_z are the longitudinal, lateral, and vertical turbulence intensity, respectively, and U_{rms}, V_{rms}, and W_{rms} denote the velocity fluctuations in the corresponding directions.

Regarding turbulence length scales, two common calculation methods are the autocorrelation method [48] and the Von Karman spectral fitting method [49]. The autocorrelation method provides an estimate of the average vortex size in a turbulent wind field, and value by the Von Karman spectral fitting method is generally half of that by the autocorrelation method [9]. In this paper, the autocorrelation method is used to determine the turbulence length scale.

There are nine turbulent length scales corresponding to the three directions related to the longitudinal, lateral, and vertical fluctuating velocity components, i.e., u, v, and w. For example, L_u^x, L_u^y, and L_u^z denote the average size of vortices in the x, y, and z directions related to the longitudinal fluctuating velocity components, respectively. They are defined as:

$$L_u = \frac{1}{\sigma_u^2} \int_0^\infty R_{12}(x)\, dx, \tag{6}$$

where $R_{12}(x)$ is the cross-correlation function of the longitudinal fluctuating velocities, i.e., $u_1 = u(x_1, y_1, z_1, t)$ and $u_2 = u(x_1+x, y_1, z_1, t)$, at two different x positions, and σ_u is the variance of the longitudinal fluctuating velocity u. According to the Taylor hypothesis, if the vortex moves at the average wind speed U, the fluctuating velocity $u(x_1, t+\tau)$ can be expressed as $u(x_1 - x, \tau)$, where $x = U\tau$. Therefore, Eq. 6 can be further expressed as:

$$L_u^x = \frac{U}{\sigma_u^2} \int_0^\infty R_u(\tau)\, d\tau, \tag{7}$$

where $R_u(\tau)$ is the autocorrelation function of the fluctuating velocity $u(x_1, t+\tau)$. L_u^y and L_u^z are calculated similarly.

In addition to the turbulence representations, the turbulence generation method in numerical studies is described. To impose specific turbulence conditions at the inlet, the STG method is employed in this study. The STG method generates time-dependent inlet conditions by superimposing a vector of synthetic velocity fluctuations onto the initial steady velocity field. Consequently, the velocity vector at a point $\mathbf{r} = \{x,\ y,\ z\}$ of an inlet boundary condition is specified as:

$$\mathbf{U}(\mathbf{r}, t) = \mathbf{U}_{\text{Inlet, mean}}(\mathbf{r}) + \mathbf{u}'(\mathbf{r}, t), \quad (8)$$

where $\mathbf{U}_{\text{Inlet, mean}}(\mathbf{r})$ is the mean velocity vector at the inlet, and $\mathbf{u}'(\mathbf{r}, t)$ is the vector of synthetic velocity fluctuations. More detailed information regarding the STG method and the definitions of symbols can be found in the reference [23].

2.5. Inflow turbulence conditions

To investigate the impact of inflow turbulence, ten cases with varying inflow turbulence conditions are simulated, with turbulence intensity ranging from 2% to 9% and turbulence length scale from 0.37H to 1.04H. The details of the inflow turbulence conditions for each case are listed in Table 2. The first case serves as the Baseline, featuring a uniform inflow inlet without using the STG method. The turbulence intensity and turbulence length scale in the table are calculated at the reference point, marked red in Figure 6. The reference point is located as close as possible to the train's front to accurately represent the actual turbulent inlet conditions, while maintaining sufficient distance to avoid interference from the train. The height of the point is sufficient to minimize ground effects, with its selection based on trends in both longitudinal and vertical turbulence values.

Figure 7 shows the turbulence intensity and length scale of selected cases, measured at the 21 reference points marked in Figure 6, distributing along the flow direction on the middle plane. The imposed turbulence intensity and length scale at the inlet are observed to decay at different rates as the flow moves downstream, particularly in cases with high turbulence intensity. Then subsequent flow field comparison results demonstrate the direct impact of the turbulent conditions on the flow surrounding the HST.

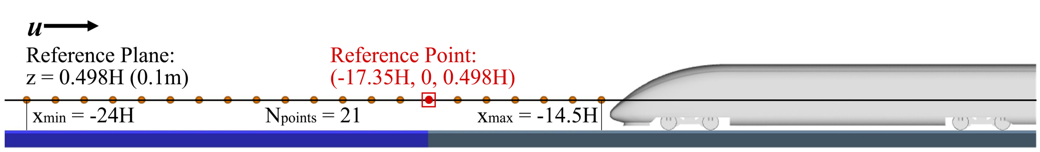

Figure 6: The location of the reference plane and points on the symmetry plane.

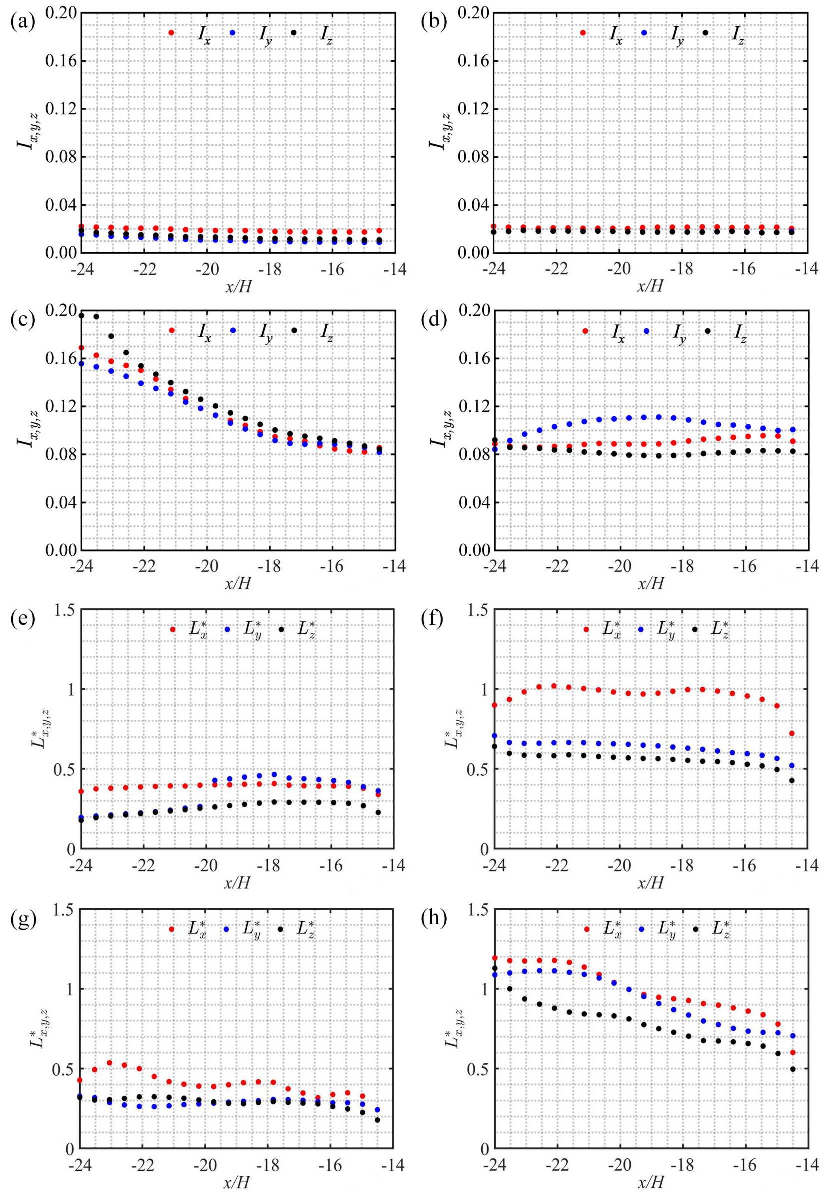

Figure 7: The calculation results of turbulence intensity and turbulence length scale along the flow direction at the longitudinal symmetry line of 0.1m height from the origin are as follows: varying turbulence intensity: (a) Ix02_L040H; (b) Ix02_L100H; (c) Ix09_L037H; (d) Ix09_L091H; varying turbulence length scale: (e) Ix02_L040H; (f) Ix02_L100H; (g) Ix09_L037H; (h) Ix09_L091H.

Table 2: The inflow turbulent conditions for the ten numerical cases.

No.	**Case name**	**Turb. intensity I_x**	**Turb. length scale L_u^x**
1	Baseline	——	——
2	Ix02_L040H	2%	0.40H
3	Ix02_L051H	2%	0.51H
4	Ix02_L100H	2%	1.00H
5	Ix04_L038H	4%	0.38H
6	Ix06_L104H	6%	1.04H
7	Ix07_L038H	7%	0.38H
8	Ix09_L056H	9%	0.56H
9	Ix09_L091H	9%	0.91H
10	Ix09_L037H	9%	0.37H

Figure 8 presents the instantaneous velocity distribution on the plane $z = 0.175H$. It can be observed that for low turbulence intensity (2%, Figure 8b), the changes in the velocity field are not significant, though the introduction of turbulence components can still be seen. As the turbulence intensity further increases (9%, Figure 8c-d), noticeable velocity fluctuations are introduced into the flow domain by STG, resulting in increased non-uniformity. Additionally, the change in turbulence length scale is clearly reflected, with larger turbulence length scales leading to larger vortex structures, particularly upstream of the HST. These observations demonstrate the effectiveness, accuracy, and controllability of the STG method in introducing turbulence for the numerical cases presented in this study.

3. Results and discussion

In this section, the influence of two key turbulence representative parameters, turbulent intensity (Section 3.1) and length scale (Section 3.2), on the aerodynamic characteristics of HSTs in operation are separately presented and discussed. For each of them, the changes in aerodynamic forces, boundary layer characteristics, and pressure distribution are examined in detail.

3.1. Turbulence intensity

3.1.1. Aerodynamic forces

The analysis of aerodynamic forces begins with the time-averaged integral force coefficients, which change along with the turbulence intensity on

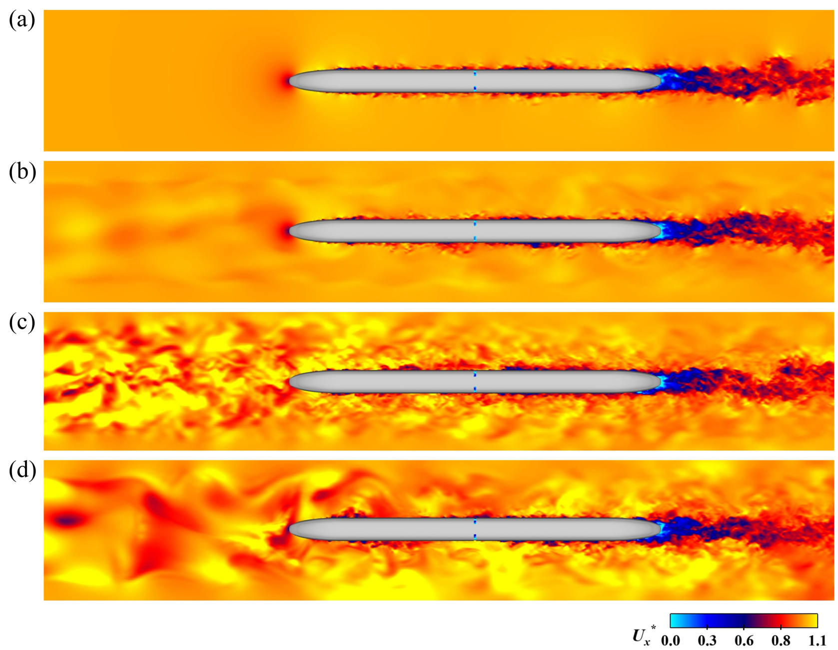

Figure 8: The instantaneous velocity distribution of plane z=0.175H: (a) Baseline; (b) Ix02_L100H; (c) Ix09_L037H; (d) Ix09_L091H.

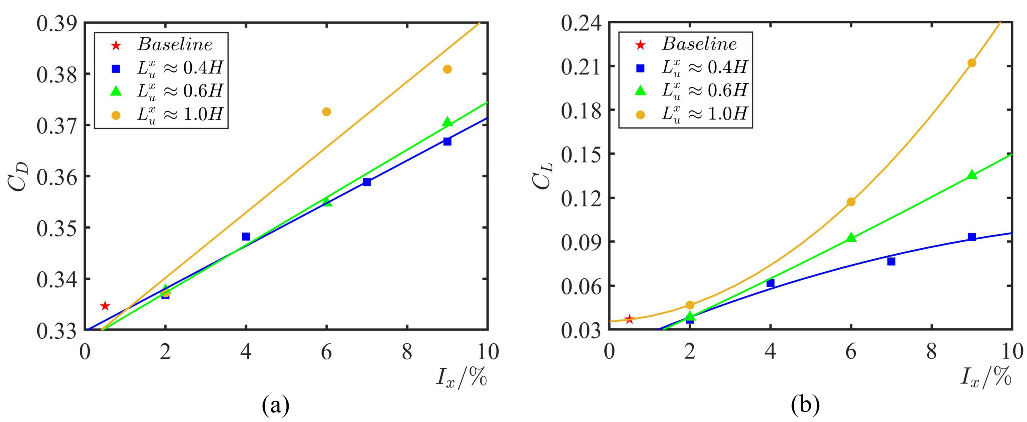

Figure 9: Distribution of time-averaged integral force coefficients with turbulence intensity: (a) drag coefficient (C_D); (b) lift coefficient (C_L).

different length scales, shown in Figure 9. Trends in drag and lift coefficients across three turbulence length scales ($L_u^x \approx 0.4H$, $L_u^x \approx 0.6H$, $L_u^x \approx 1.0H$, marked with different labels) are studied in distinct groups.

First, and most notably, both the drag and lift coefficients exhibit an increasing trend in responding to rising turbulence intensity across all turbulence length scales. For the drag coefficient, the increase follows a more linear pattern, with a higher growth rate observed at larger turbulence length scales ($L_u^x \approx 1.0H$). Specifically, the larger deviation of the drag coefficient from the regression line at $I_x = 6\%$ and $I_x = 9\%$ can be attributed to the larger turbulence length scale at $I_x = 6\%$ (1.04H) and the smaller length scale at $I_x = 9\%$ (0.91H). However, for the lift coefficient, the growth rate with respect to turbulence intensity is not constant and is influenced by the turbulence length scale. When the turbulence length scale is relatively small ($L_u^x < 0.6H$), the trend follows a sub-linear pattern, whereas under large-scale conditions ($L_u^x > 0.6H$), it demonstrates a super-linear behavior. This disparity indicates that the turbulence length scale has a more pronounced effect on lift than drag. Given that turbulence intensity has a more significant impact at large turbulence length scale ($L_u^x \approx 1.0H$), the subsequent analysis focus on this scale, especially case 4 (Ix02_L100H), case 6 (Ix06_L104H), and case 9 (Ix09_L091H).

To better understand the mechanisms through which turbulence intensity influences the aerodynamic forces on the train, it is crucial to examine individual carriages separately. Consequently, the subsequent analysis concentrates on the aerodynamic force trends for both the head and tail carriages under varying turbulence intensities, aiming to determine which carriage primarily contributes to the overall aerodynamic response to turbulence intensity. Figure 10 illustrates the changes in aerodynamic force coefficients, relative to the Baseline, for the two carriages under three different turbulence intensity conditions. The results of time-averaged drag coefficient (Figure 10a) indicate that drag for both the head carriage and the tail carriage increase as turbulence intensity rises. Compared with the Baseline, the increase in drag for the tail carriage is more pronounced than for the head carriage. At low turbulence intensity ($I_x = 2\%$), the drag increment remains minimal, whereas at high turbulence intensity ($I_x = 9\%$), the total drag coefficient increases by 46 counts (+14%). At $I_x = 6\%$, this trend of increasing drag become evident, with the total drag coefficient rising by 38 counts (+11%).

On the other hand, regarding the time-averaged lift coefficient (Figure 10b), turbulence intensity exerts a more significant impact on lift than on drag, aligning with previous results for the entire train set. At low turbulence intensity, similar to the drag results, the increment in lift is negligible.

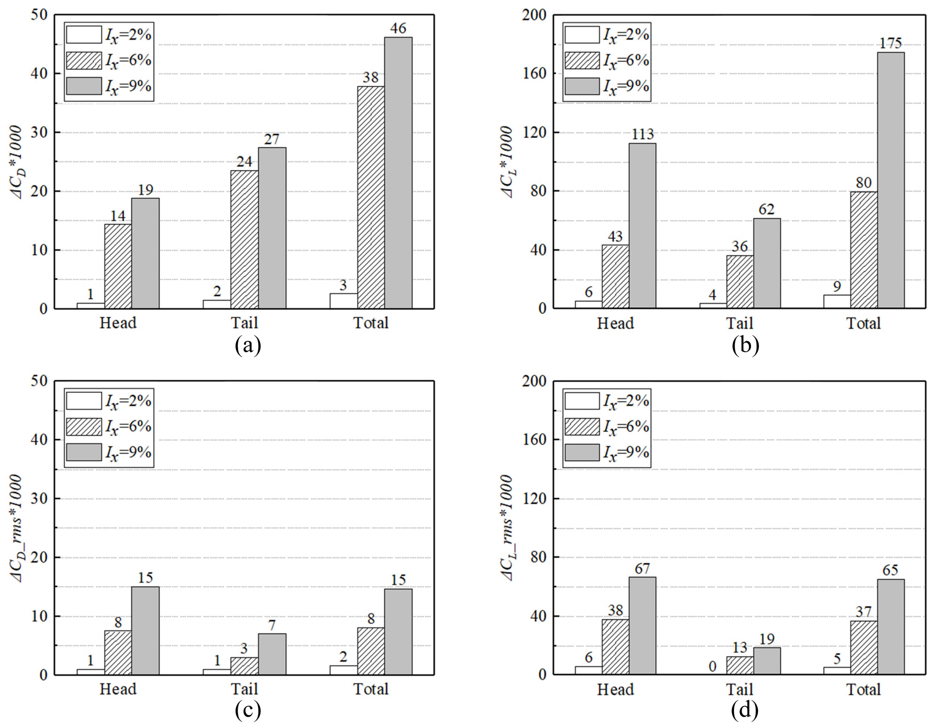

Figure 10: The increment of aerodynamic force coefficients of the two carriages at large turbulence length scale under different turbulence intensities: (a) time-averaged C_D; (b) time-averaged C_L; (c) RMS of C_D; (d) RMS of C_L.

However, at medium and high turbulence intensities, the total lift coefficient increases by factors of 2.2 and 4.7, respectively. Notably, in contrast to the drag results, turbulence intensity exerts a more substantial effect on the lift of the head carriage than on the tail carriage.

Moreover, Figure 10c-d illustrates the increments in the root mean square (RMS) of the drag and lift coefficients, which represent the fluctuation levels of aerodynamic forces. Both the RMS of drag and lift increase with rising turbulence intensity, with the head carriage exhibiting a pronounced increase than the tail carriage. As expected, under high turbulence intensity conditions, alternating loads are exerted on the carriage surface, leading to stronger fluctuations in aerodynamic forces, which may further affect the operating smoothness of the HST under turbulent wind condition.

To further investigate the variations in aerodynamic forces for each individual train component, particularly focusing on the bogie structures, the increments in aerodynamic force coefficients of more train components are computed and presented in Figure 11. Figure 11a illustrates that as the turbulence intensity increases, the C_D of the head carriage primarily increases in the first bogie cavity (C1) and the second bogie (B2), while that of the head body exhibits minimal change. The C_D of all components of the tail carriage increases with rising turbulence intensity, with the most significant increase observed in the tail body. Notably, for most components of the tail carriage, particularly in the fourth bogie region (including bogie and cavity), the drag-increasing effect of the turbulence intensity is prominent up to $I_x = 6\%$, beyond which further increases in turbulence intensity do not result in significant changes in drag. Regarding C_L (Figure 11b), as the turbulence intensity increases, the C_L of the head body increases significantly, followed by that of the tail body. In addition, the third bogie cavity demonstrates a distinct contribution to the increase in lift. For the RMS of C_D and C_L (Figure 11c-d), the main contributing regions for the increase in drag fluctuations are the head body H_b and the first bogie cavity C1, with the trend of lift fluctuations closely mirroring that of drag.

To clarify the mechanism underlying the increase in aerodynamic drag, it is further decomposed into pressure drag and viscous drag. Their devel-

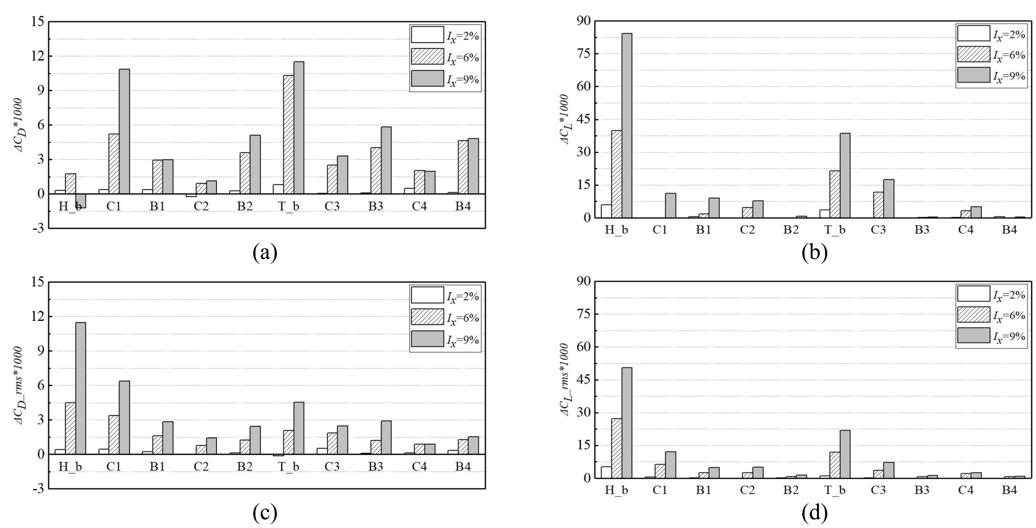

Figure 11: The increment of aerodynamic force coefficients of train components at large turbulence length scale: (a) time-averaged C_D; (b) time-averaged C_L; (c) RMS of C_D; (d) RMS of C_L. The representing train components of abbreviations $C1$, $B1$, $C2$, $B2$, $C3$, $B3$, $C4$, $B4$ are given in Figure 1.

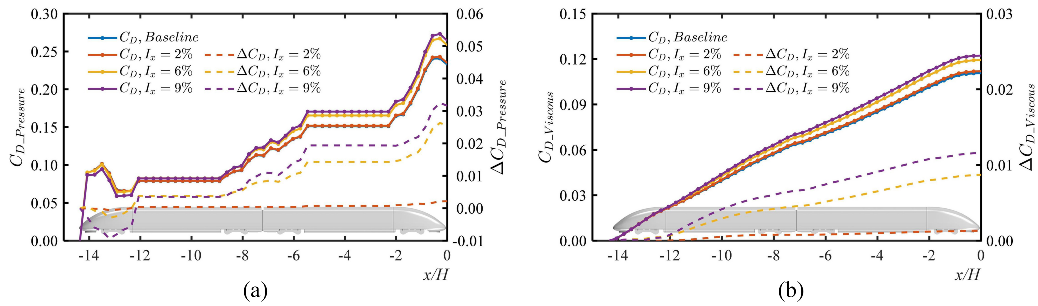

(a) (b)

Figure 12: Decomposed cumulative drag coefficients along the flow direction at large turbulence length scale of $L_u^x \approx$ 1.0H under varying turbulence intensity: (a) pressure drag C_{D_Pressure}; (b) viscous drag C_{D_Viscous}.

opment on the head body along the flow direction is shown in Figure 12, including absolute values (solid lines, left axis) and the variance from Baseline (dashed lines, right axis).

The development of pressure drag is first addressed, shown in Figure 12a. From its absolute values along the flow direction for the Baseline, it is evident that the contributions of the three non-smooth regions to the pressure resistance are essentially equal. In other words, each of nose and bogie structure of the head carriage, the tail carriage, and the carriage junction region, contributes approximately 0.08 to the pressure drag coefficient. Regarding the impact of turbulence conditions, when the turbulence intensity is low ($I_x = 2\%$), only a slight variance is observed. However, as turbulence intensity increases, the influence on pressure drag becomes more significant. Among these changes in C_D, when the turbulence intensity increases from 2% to 6%, the main contribution region starts behind the second bogie structure. On the one hand, it is noteworthy that the variance in cumulative pressure drag rises rapidly at the non-smooth carriage junction and the third bogie region. On the other hand, the rear region ($x > -2H$) also exhibits significant influence, where flow detachment occurs and the wake development begins.

Further increasing the turbulence intensity to 9% does not produce such a large variance, during which, this variance is mainly due to the carriage junction and the third bogie structures. Although the values of the two are also separated at the front of the carriage ($x < -12H$), the effects of the drag-enhancing and drag-reducing regions counteract each other. Finally, the cumulative pressure drag of $I_x = 6\%$ and $I_x = 9\%$ becomes the same at the straight section of the head carriage. It is concluded that the structure of the carriage junction has a very strong influence on the aerodynamic drag under high turbulence intensity conditions ($I_x \geq 6\%$) compared to other components. In order to better reduce the drag increasing under wind conditions with large turbulence intensity, it is crucial to smoothly connect neighboring carriages, or to use active or passive flow control approaches for aerodynamic drag reduction in this region.

Figure 12b illustrates the development of the viscous drag coefficient. From the absolute values, it is evident that viscous drag consistently rises along the flow direction due to the skin friction. The case under $I_x = 2\%$ continues to exhibit behavior similar to the Baseline, with an insignificant increase in viscous drag. As the turbulence intensity increases from 2% to 6%, the difference emerges at $x = -12H$ and subsequently grows linearly along the flow direction. The effect of further increasing the turbulence intensity is concentrated in the straight section of the head carriage, likely due to changes in the boundary layer state.

Figure 13 illustrates the development of the lift coefficient along the flow direction under conditions of a large turbulence length scale ($L_u^x \approx 1.0H$). First, negative lift (downforce) is generated at the windward curved section (front edge) of the head carriage, while a substantial increase in lift occurs at the curved section of the tail carriage, consistent with expectations. Additionally, lift is generally enhanced in the bogie regions, particularly in the first and third bogie sections. Conversely, the straight sections of the carriage result in a reduction in lift, with the most rapid decline occurring as

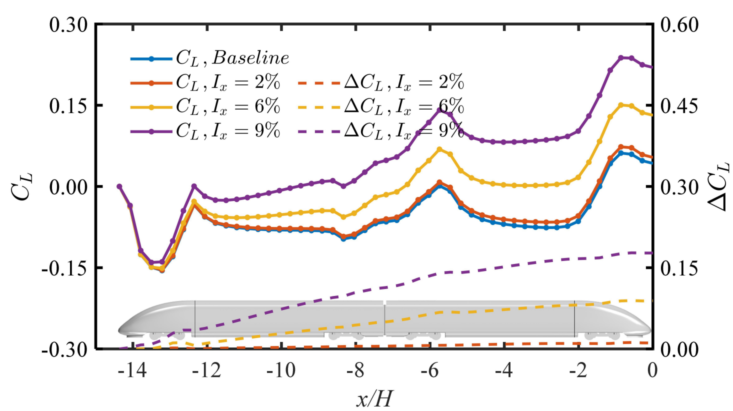

Figure 13: Cumulative lift coefficients along the flow direction at large turbulence length scale of $L_u^x \approx 1.0$H under varying turbulence intensity.

the airflow transitions into the straight section.

As with drag, the influence of turbulence intensity on lift is also examined. It is evident that, as turbulence intensity increases, lift increases across nearly all regions. For $I_x = 2\%$, the increase in lift is relatively modest, whereas higher turbulence intensities exert a pronounced effect. In the cases of both Baseline and $I_x = 2\%$, lift remains negative throughout most regions, with the exception of the rear edge of the tail carriage. Under higher turbulence intensities, the cumulative drag becomes positive after passing through the first bogie region. More importantly, significant disparities are observed in the final total lift coefficients: at high turbulence intensity ($I_x = 9\%$), the lift coefficient exceeds the Baseline by more than four times, while at moderate turbulence intensity ($I_x = 6\%$), the lift is more than twice that of the Baseline. These findings are consistent with the conclusions presented in Figure 9.

The analysis and discussion presented above are based on the conditions associated with a large turbulence length scale ($L_u^x \approx 1.0H$). To further investigate the effects under different turbulence scales, Figure 14 presents the decomposed drag under a smaller turbulence length scale ($L_u^x \approx 0.40H$). The overall trends observed at different turbulence intensities are similar to those previously discussed for the large turbulence length scale. However, the influence of turbulence intensity is notably weaker under the smaller turbulence length scale.

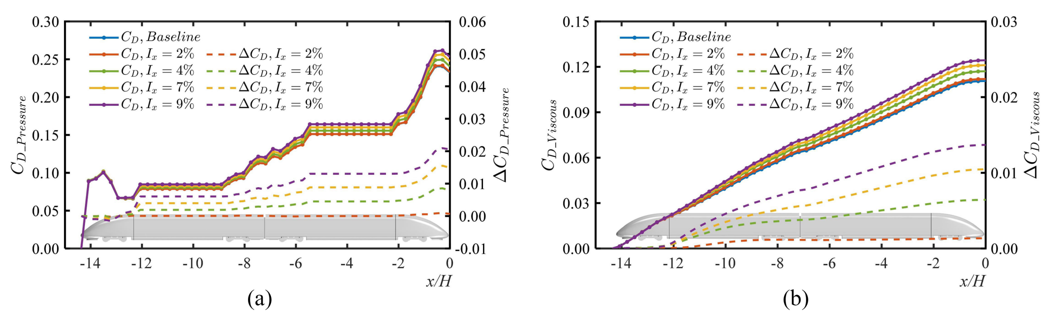

Figure 14: Decomposed cumulative drag coefficients along the flow direction at small turbulence length scale of L_u^x≈0.40H under varying turbulence intensity: (a) pressure drag C_{D_Pressure}; (b) viscous drag C_{D_Viscous}.

3.1.2. Boundary layer

From the previous discussion in Section 3.1.1, it is observed that the viscous drag increases with higher turbulence intensity. In order to further study the formation mechanism of viscous drag, the boundary layer is studied, whose formation and development directly determine the magnitude and distribution of viscous drag exerted on the train surface. To quantitatively study the boundary layer, the displacement thickness δ_1, momentum thickness δ_2 and shape factor H_{12} are introduced, which are defined as:

$$\delta_1 = \int_0^\infty \left(1 - \frac{u}{U_\infty}\right) dy; \tag{9}$$

$$\delta_2 = \int_0^\infty \frac{u}{U_\infty}\left(1 - \frac{u}{U_\infty}\right) dy; \tag{10}$$

$$H_{12} = \frac{\delta_1}{\delta_2}, \tag{11}$$

where u is the time-averaged velocity at a given point in the boundary layer, and U_∞ is the free-stream velocity outside the boundary layer. Among them, δ_1 describes the equivalent wall offset distance that represents the blockage effect of the boundary layer on fluid volumetric flow rate, while δ_2 focuses on the equivalent wall offset distance for momentum loss caused by boundary layer. The quotient of them two (H_{12}) represents the fullness of the boundary layer velocity profile, and lower H_{12} means a fuller velocity profile and larger the velocity gradient. Generally high H_{12} indicates a laminar boundary layer, with a relatively low viscous drag, while low H_{12} is obtained for turbulent boundary layer. Figure 15 shows the displacement thickness δ_1 and

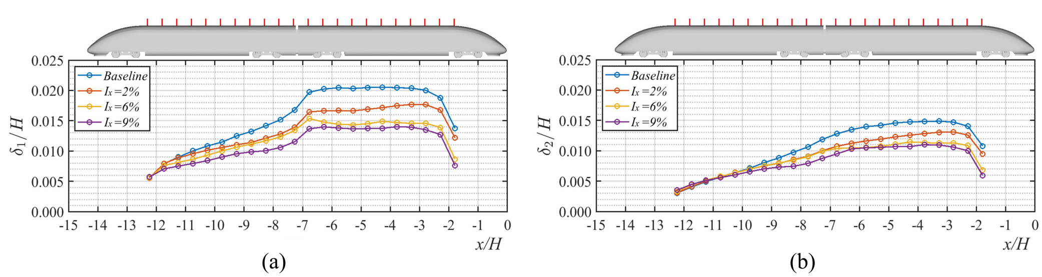

Figure 15: Displacement thickness and momentum thickness along the longitudinal symmetry line at the top of the train under varying turbulence intensity: (a) displacement thickness δ_1; (b) momentum thickness δ_2.

momentum thickness δ_2 along the longitudinal symmetry line at the top of the train.

It is evident that both the displacement thickness δ_1 and momentum thickness δ_2 of the boundary layer increase along the flow direction, indicative of a typical development of boundary layer. However, at the rear section of the tail carriage, prior to entering the curve section, the boundary layer thickness decreases, likely due to the contraction effect induced by the streamlined tail, which modifies the surrounding flow. In this region, a decrease in pressure and an increase in flow velocity occur, resulting in reduced momentum exchange, which ultimately suppresses and reverses the further development of the boundary layer. In addition, a comparison between the two thickness indicators reveals that δ_1 tends to stabilize in the straight section of the tail carriage, while δ_2 continues to increase, albeit at a slower rate. Consequently, after the development stage of the boundary layer along the head carriage and the subsequent disturbance at the carriage junction, the volume of fluid contained within the boundary layer remains largely unchanged. However, momentum exchange between the fluid inside and outside the boundary layer persists, leading to a continued transition toward a more turbulent state. Regarding the impact of turbulence intensity, the final thickness of the boundary layer is essentially the same under different turbulence intensities. Although, a higher turbulent intensity leads to thinner initial and developing boundary layer.

The shape factors, depicted in Figure 16, show a consistent decrease along the flow direction, signifying that the flow state within the boundary layer progressively transitions toward turbulence as the boundary layer develops.

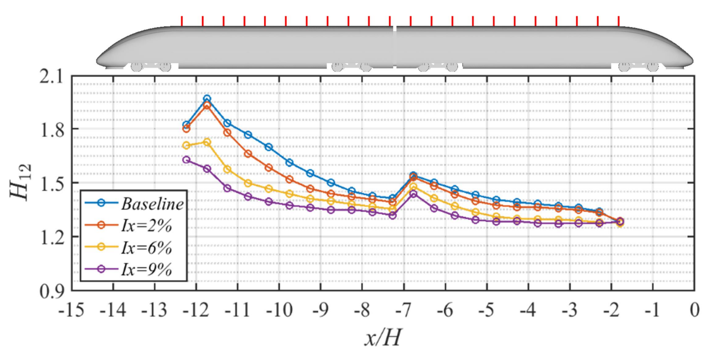

Figure 16: Shape factor H_{12} along the longitudinal symmetry line at the top of the train under varying turbulence intensity.

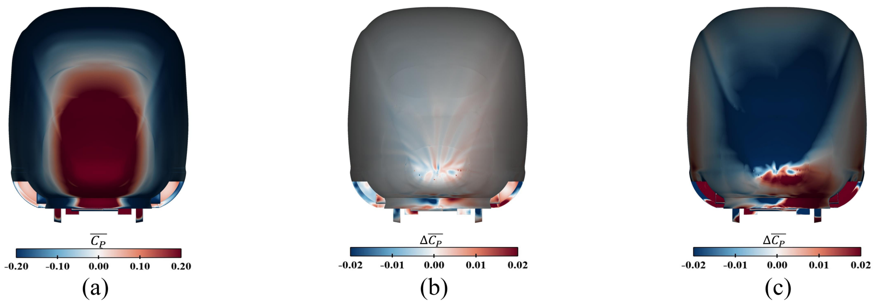

Figure 17: Time-averaged surface pressure coefficient distribution of the front of the head carriage: (a) time-averaged C_P of Baseline; (b) $\Delta C_{P(2\%)}$; (c) $\Delta C_{P(9\%)}$.

At the junction between the two carriages, the separation and reattachment of the airflow temporarily disrupt the development of the boundary layer. Additionally, it is apparent that the shape factor decreases with increasing turbulence intensity, reflecting a steeper velocity gradient under high turbulence conditions. This in turn leads to a higher viscous drag when compared to low turbulence conditions, as shown in Figure 12b.

3.1.3. Pressure distribution

The surface pressure distribution of HST, which is also affected by the incoming turbulence, can be used to locate the source of pressure drag, and provide valuable insights for studies of the wind load of the carriage.

Figure 17 shows the front view of the time-averaged surface pressure coefficient on the head carriage under the Baseline and two turbulence conditions ($I_x = 2\%$ and $I_x = 9\%$). To clearly illustrate the differences, the raw value is used for the baseline, while the surface distributions of the pressure difference, relative to the Baseline, are computed for the turbulence cases. The surface pressure coefficient difference between the turbulence cases and the Baseline is defined as:

$$\Delta C_{P(2\%)} = C_P|_{I_x=2\%} - C_P|_{\text{Baseline}}, \tag{6}$$

where $\Delta C_{P(2\%)}$ is the pressure difference between $I_x = 2\%$ and the Baseline. The pressure difference under other conditions is defined in the same way.

For the low turbulence intensity case ($I_x = 2\%$), the surface pressure on the front of the head carriage shows minimal variation compared to the Baseline, resulting in only a slight difference in aerodynamic forces. In contrast, under high turbulence intensity ($I_x = 9\%$), the pressure distribution on the front of the head carriage undergoes significant changes: the pressure on the lower surface increases, while that on the upper surface decreases. Consequently, this configuration leads to lower drag and higher lift in this region.

Figure 18 presents the instantaneous surface pressure coefficient distribution on the head carriage for both the Baseline and the high turbulence intensity case ($I_x = 9\%$). The Baseline case exhibits a generally symmetric pressure distribution. However, under high turbulence intensity, the flow field becomes notably asymmetric, resembling a crosswind effect. This asymmetry results in airflow impacting the front of the train at a slight yaw angle, diminishing the positive pressure area and thereby reducing the head pressure. Simultaneously, due to the crosswind effect, the side flow accelerates, leading to a substantial decrease in side pressure. Simultaneously, the crosswind effect accelerates the side flow, leading to a substantial decrease in side

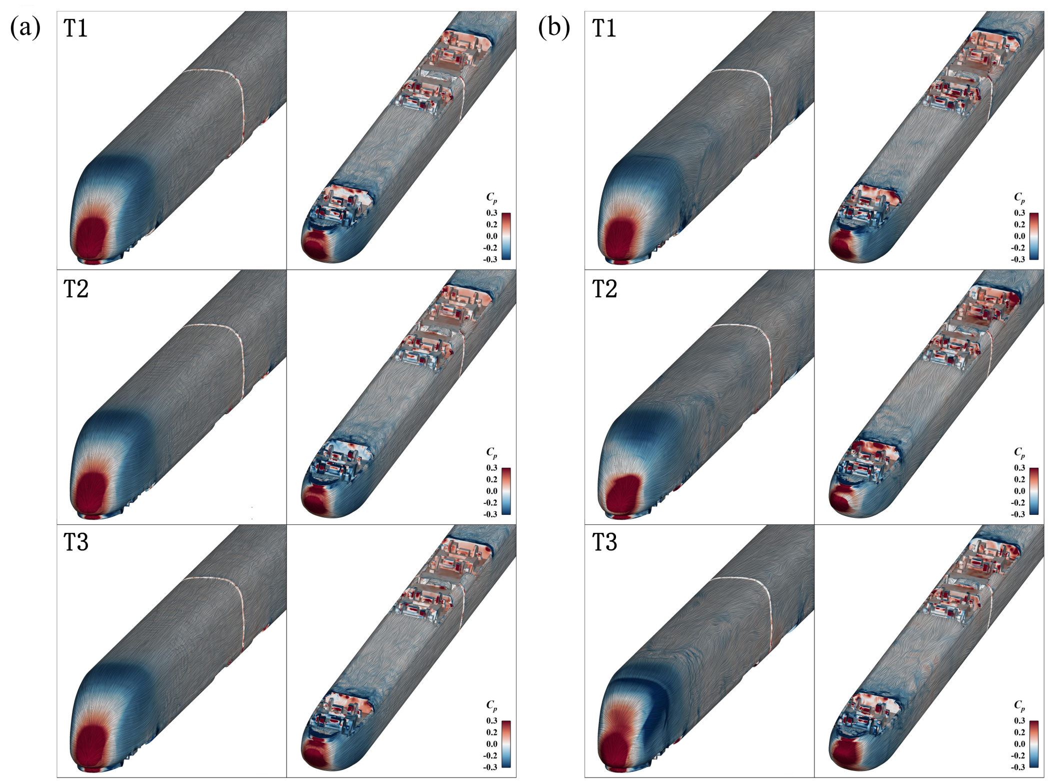

Figure 18: Instantaneous surface pressure coefficient distribution of the front of the head car: (a) Instantaneous C_P of Baseline; (b) Instantaneous C_P of I_x=9%.

pressure. This asymmetry in side pressure allows more flow to enter the bogie cavity, increasing the pressure near its rear edge.

Figure 19 presents the time-averaged surface pressure coefficient on the bottom of the train for the Baseline, $I_x = 2\%$, and $I_x = 9\%$. Notably, for the Baseline case, the pressure decreases substantially near the trailing edge of the bogie cavity in the straight section, due to flow separation, which reduces lift, in accordance with the results shown in Figure 13. Additionally, as the flow velocity decreases in the straight section of the bottom, the pressure rises to nearly zero before entering the second bogie cavity, leading to an increase in lift. Under high turbulence ($I_x = 9\%$), the pressure distribution on the bottom surface in the straight section is higher than in the Baseline case, which likely accounts for the observed increase in lift force. The pressure in the four bogie cavities also increases. A comparison of the four bogie cavities reveals that the first cavity experiences the highest pressure difference $\Delta C_{P(9\%)}$ among them four. From these results, it is deduced

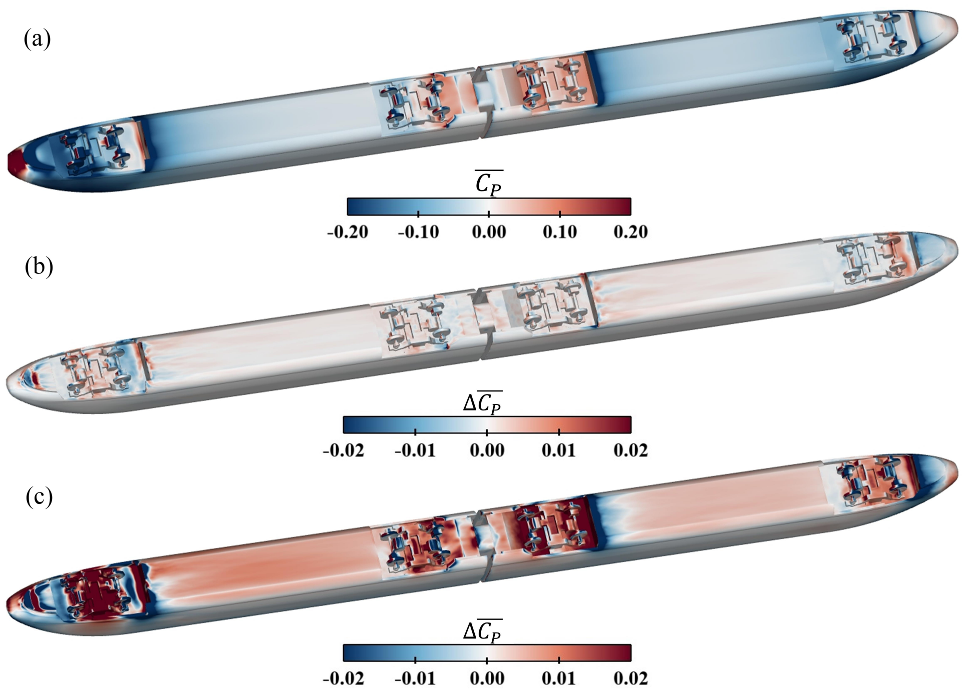

Figure 19: Time-averaged surface pressure coefficient distribution of the bottom of the train: (a) time-averaged C_P of Baseline; (b) $\Delta C_{P(2\%)}$; (c) $\Delta C_{P(9\%)}$.

that, under high turbulence intensity, lift at the front of the head carriage and in the straight section of the bottom increases significantly. In contrast, for low turbulence intensity, lift remains nearly unchanged compared to the Baseline, with $\Delta C_{P(2\%)}$ being less than 0.002 at most locations. This finding corroborates the observation that lift increases in a nearly parabolic fashion with turbulence intensity, as indicated in Figure 9b.

From the above analyses, it is evident that the influence of the bogie cavity on the aerodynamic forces of the HST is substantial. To further elucidate the flow characteristics within the bogie cavities, Figure 20 presents the turbulent kinetic energy in the first bogie region under different turbulence intensities. As the turbulence intensity increases, the turbulent kinetic energy on both sides of the bogie increases correspondingly. This intensification of flow mixing within the shear layer between the bogie cavity and the underbody airflow facilitates a greater influx of air into the bogie cavity, in line with the high-pressure regions depicted in Figure 19. This variation in turbulent kinetic energy likely enhances the fluid-solid interaction, contributing to the changes in pressure observed. Additionally, the increase in

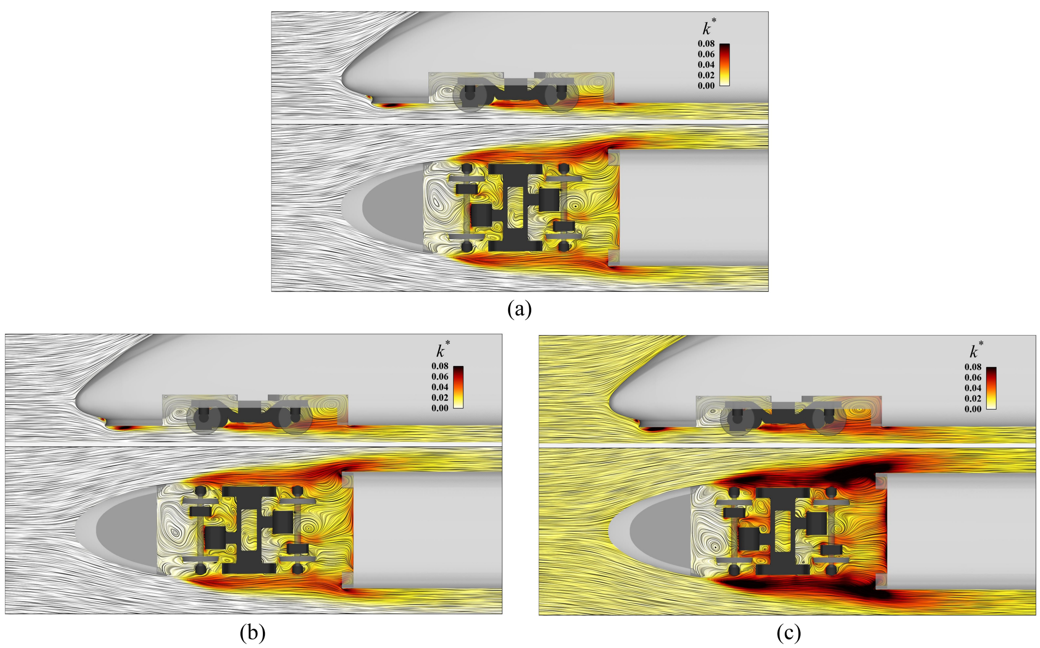

Figure 20: Turbulent kinetic energy distribution in the first bogie region: (a) Baseline; (b) $I_x = 2\%$; (c) $I_x = 9\%$.

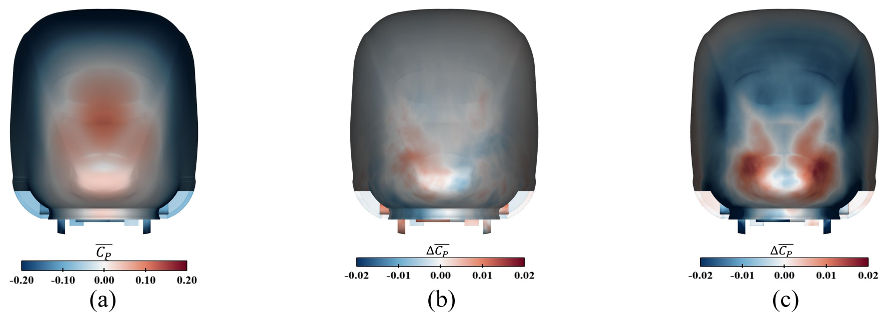

Figure 21: Time-averaged surface pressure coefficient distribution of the rear of the tail carriage: (a) Baseline; (b) $I_x = 2\%$; (c) $I_x = 9\%$.

turbulent kinetic energy near the rear surface of the bogie cavity further suggests that these changes in pressure are driven by enhanced turbulence and flow interactions in this region.

Figure 21 shows the time-averaged surface pressure coefficient distribution of the rear of the tail carriage for the Baseline, $I_x = 2\%$ and $I_x = 9\%$ cases. For the Baseline case, as the airflow enters the curve section, the surface pressure becomes negative, transitioning to a positive value near the tail nose, consistent with the results shown in Figures 5b and 14a Similar to the previous results, low turbulence intensity exerts minimal influence. However, under high turbulence intensity $I_x = 9\%$, the upper surface, as well as the upper half of the side surfaces, induces more negative pressure, thereby increasing pressure drag. Furthermore, an annular high-pressure zone forms around the nose edge, which may indicate specific flow topology structure during wake formation.

3.2. Turbulence length scale

During the operation of HST, varying turbulence length scales are typically encountered due to diverse terrain and different atmospheric boundary layer conditions. This section examines the influence of turbulence length scale on HST by comparing aerodynamic forces and boundary layer development under different turbulence length scale conditions. The surface pressure distributions are not further investigated as they show very similar trends as varying turbulence intensity.

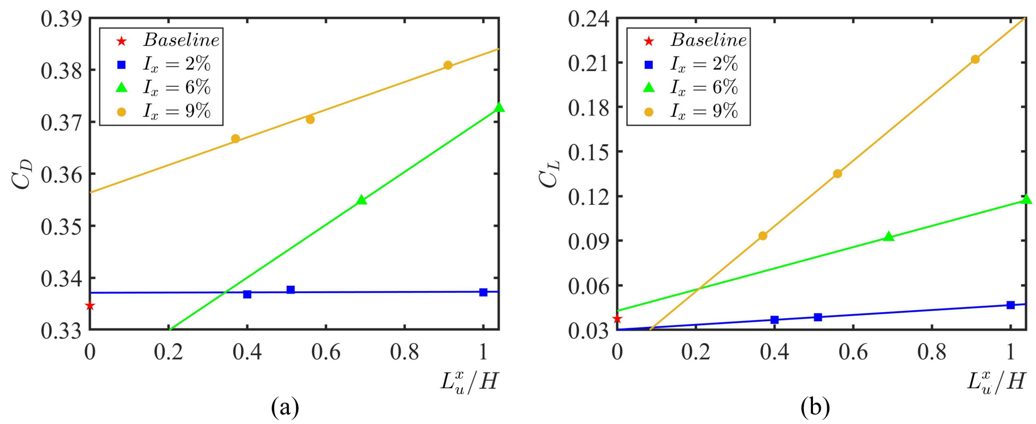

Figure 22: Distribution of time-averaged integral force coefficients with turbulence length scale: (a) drag coefficient (C_D); (b) lift coefficient (C_L).

3.2.1. Aerodynamic forces

Figure 22 presents the distribution of integral aerodynamic coefficients as a function of turbulence length scale across varying turbulence intensities. The results indicate that both drag and lift coefficients increase with increasing turbulence length scale, irrespective of turbulence intensity. Under low turbulence intensity conditions ($I_x = 2\%$, blue curve), the effect of turbulence length scale on drag and lift coefficients is minimal. Consequently, this section focuses on results obtained under high turbulence intensity, specifically case 8 (Ix09_L056H), case 9 (Ix09_L091H), and case 10 (Ix09_L037H), all characterized by a turbulence intensity of 9%.

Figure 23 illustrates the relative increase in aerodynamic force coefficients with RMS for the head carriage, tail carriage, and entire train set under different turbulence length scale conditions, relative to the Baseline. The findings reveal that turbulence length scale affects drag and lift forces, as well as their fluctuations, for the head carriage, tail carriage, and the entire train set in a manner similar to that observed with increasing turbulence intensity. Larger turbulence length scales result in increased drag, lift, and their fluctuations.

However, when analyzing specific decomposed components (Figure 24), where the carriages are further divided into bodies, bogies, and bogie cavities, the influence of turbulence length scale diverges notably from that of turbulence intensity. Specifically, the drag on the head body decreases monotonically as the turbulence length scale increases, whereas the drag on the

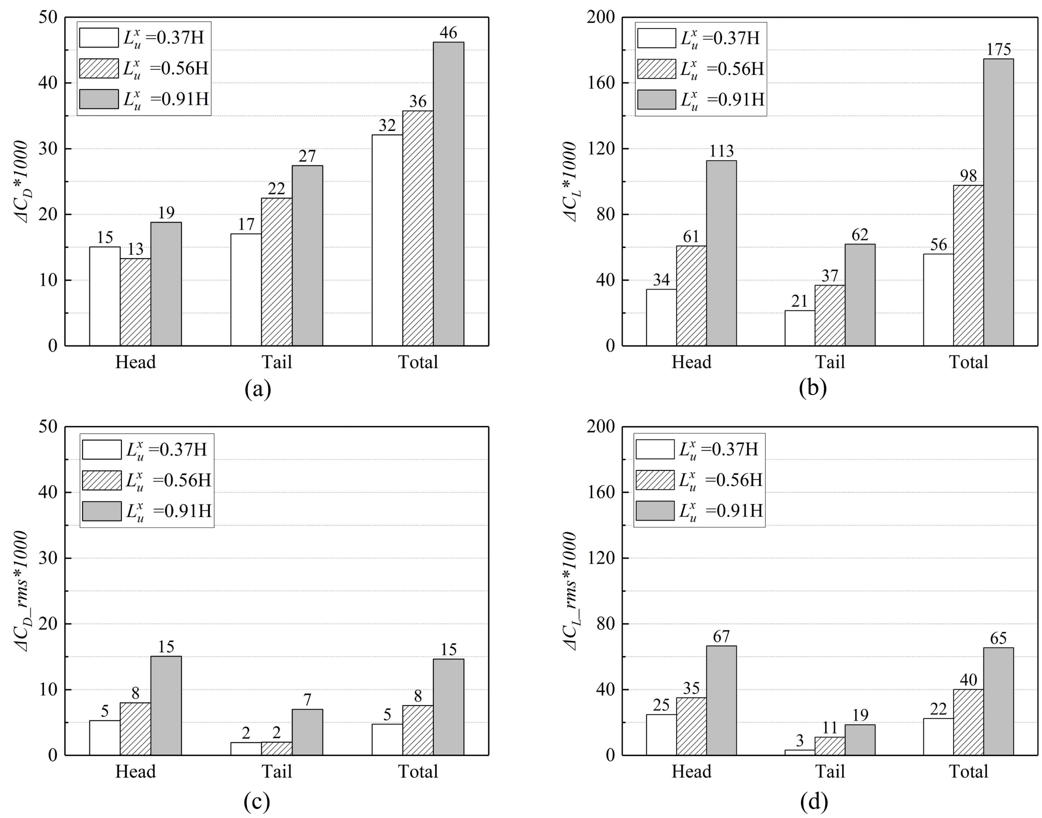

Figure 23: The increment of aerodynamic force coefficients of the two carriages at $I_x = 9\%$: (a) time-averaged C_D; (b) time-averaged C_L; (c) RMS of C_D; (d) RMS of C_L.

tail body changes little. In terms of lift, as well as RMS of both drag and lift, the trends closely resemble those observed under varying turbulence intensity. Thus, the effect of longer turbulence length scales on aerodynamic forces is, in many respects, equivalent to the effect of higher turbulence intensity.

To elucidate the observed differences in drag, decomposed cumulative drag coefficients along the flow direction are plotted in Figure 25. The pressure drag exhibits a trend similar to that observed under increasing turbulence intensity: as the turbulence length scale increases, the pressure drag on the curved section of the head body decreases. Conversely, the viscous drag on the head body decreases with increasing turbulence length scale, which is in contrast to the trends observed under varying turbulence intensity. For the head carriage, both the pressure drag on the curved section containing bogie structures and the viscous drag on the straight section decrease as the

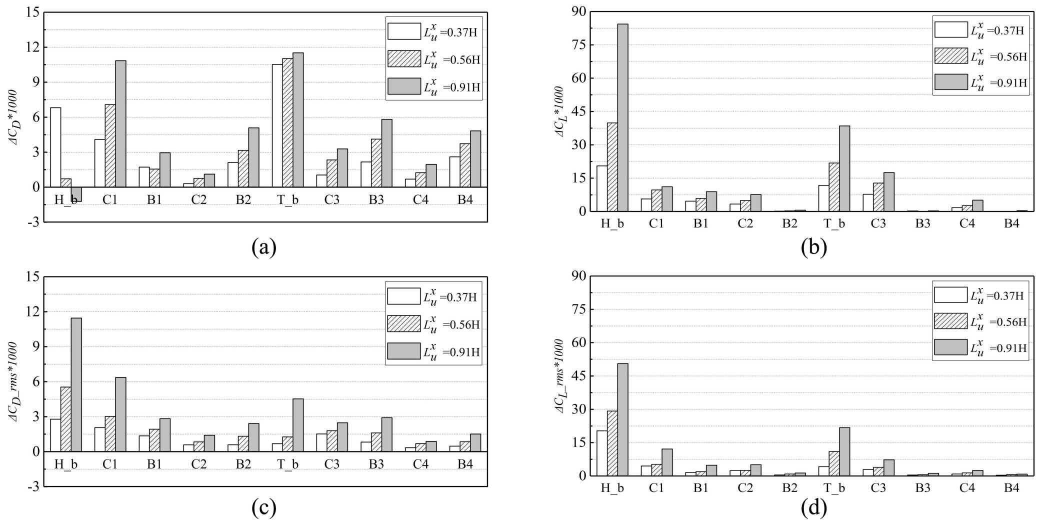

Figure 24: The increment of aerodynamic force coefficients of train components at $I_x = 9\%$ under different turbulence length scales: (a) time-averaged C_D; (b) time-averaged C_L; (c) RMS of C_D; (d) RMS of C_L. The definitions of abbreviations are the same in Figure 11.

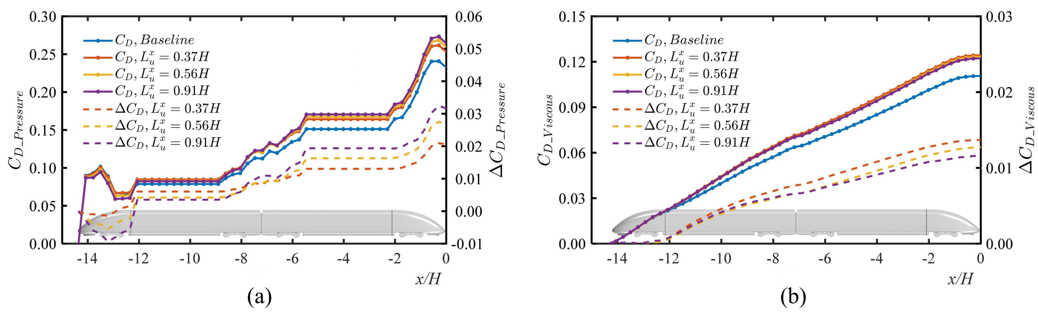

Figure 25: Decomposed cumulative drag coefficients along the flow direction at high turbulence intensity ($I_x \approx 9\%$): (a) pressure drag C_{D_Pressure}; (b) viscous drag C_{D_Viscous}.

turbulence length scale increases. Consequently, the overall drag exerted on the head carriage demonstrates a reduction trend with increasing turbulence length scale.

3.2.2. Boundary layer

Figure 26 depicts the displacement thickness (δ_1) and momentum thickness (δ_2) along the longitudinal symmetry line at the top of the train under different turbulence length scale configurations. The results indicate that the influence of turbulence length scale on boundary layer thickness is not

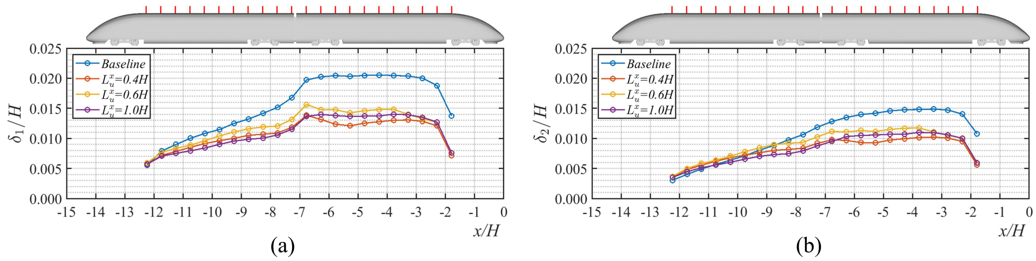

Figure 26: Displacement thickness and momentum thickness distributions along the longitudinal symmetry line at the top of the train under varying turbulence length scale: (a) displacement thickness δ_1; (b) momentum thickness δ_2.

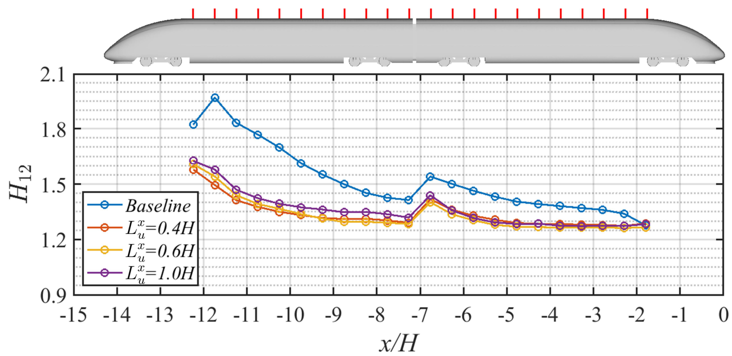

Figure 27: Shape factor H_{12} distributions along the longitudinal symmetry line at the top of the train under varying turbulence length scale.

pronounced across the three turbulence cases. However, a comparative analysis reveals that the boundary layer thickness for the $L_u^x = 0.6H$ configuration remains consistently the greatest. For the other two configurations, the boundary layer thickness on the head carriage is greater for $L_u^x = 0.4H$ compared to $L_u^x = 1.0H$, whereas the opposite trend is observed on the tail carriage. This transition occurs within the carriage junction region, likely due to changes in the turbulence state of the boundary layer.

As shown in Figure 27, the shape factors (H_{12}) on the tail carriage are relatively consistent across all three turbulence cases. This may be due to the rapid changes in fluid state in the carriage junction area. Consequently, the findings further underscore the critical role of its design. However, for $L_u^x = 1.0H$, the shape factor on the head carriage is higher than that observed in the other two cases. This discrepancy can be attributed to the larger turbulence length scale, which, under identical turbulence intensity, contains less energy in smaller-scale eddies. As we know, displacement thickness δ_1 characterizes the loss of volume flow rate, while momentum thickness δ_2 is for momentum loss by viscosity. From Figure 26, the presence of turbulence reduces both δ_1 and δ_2 by exciting the momentum exchange. Larger vortex structures affect more the outer layer of the boundary layer, thickening the boundary layer, while having less effect on the viscous sublayer. As a result, their influence on the momentum loss is less than smaller ones, leading to an increased shape factor H_{12} at larger turbulence length scales. Additionally, in contrast to the influence of turbulence intensity, the shape factor increases with the growth of turbulence length scale. Smaller turbulence length scales lead to steeper velocity gradients, thereby resulting in increased viscous drag, as shown in Figure 25b.

4. Conclusions

In this study, an Improved Delayed Detached Eddy Simulation (IDDES) method combined with the Synthetic Turbulence Generation (STG), is employed to investigate the effects of incoming turbulence on the aerodynamic characteristics of a two-carriage High-Speed Train (HST). Ten configurations of incoming turbulence, characterized by varying turbulence intensities and length scales, are simulated and analyzed. This paper provides a comprehensive examination of aerodynamic forces, pressure distributions, flow around the bogie cavities, and boundary layers in relation to these two turbulence properties. The primary conclusions are as follows:

1. Both turbulence intensity and turbulence length scale significantly influence the mean drag and lift coefficients of the train. The maximum observed increases in drag and lift coefficients are 46 counts and 175 counts, respectively, occurring under conditions of turbulence intensity at 9% and length scale at 0.91H.
2. Incoming turbulence interacts with the carriages in a manner similar to a crosswind. It weakens the aerodynamic impact on the head carriage, reducing surface pressure, which results in drag reduction and lift increase. Simultaneously, the accelerated flow around the curved section of the tail carriage decreases surface pressure, thereby increasing the pressure drag on the tail carriage.
3. Incoming turbulence increases the turbulent kinetic energy within the shear layers adjacent to the bogie cavity, intensifying the mixing between

the underbody flow and the cavity flow. This leads to a greater influx of flow into the cavity, thereby increasing drag. The intensified flow-cavity interaction reduces the underbody flow velocity and raises surface pressure, contributing to increased lift along the straight sections.

4. High turbulence intensity reduces the shape factor of the boundary layer on the train surface, leading to an steeper velocity gradient and elevated viscous drag. Conversely, larger turbulence length scales tend to increase the boundary layer shape factor.
5. The aerodynamic viscous drag acting on the train are significantly affected by the design of the carriage junction. This region induces notable changes in the flow state within the boundary layer, highlighting the importance of its aerodynamic optimization.

In summary, this paper presents a comprehensive analysis of the aerodynamic forces, boundary layer, and flow in the bogie region. Based on these current findings, our subsequent research will further focus on the impact of incoming turbulence on the unsteady wake topology with particular attention to its three-dimensional dynamic patterns, as well as corresponding variations in train slipstream characteristics.

Declarations

- **Funding:**
This work was supported by the National Natural Science Foundation of China (Grand No. 51905381) and Shanghai Key Laboratory of Aerodynamics and Thermal Environment Simulation for Ground Vehicles (Grant No. 23DZ2229029).

- **Acknowledgements:**
The computations were enabled by resources provided by the National Academic Infrastructure for Supercomputing in Sweden (NAISS), partially funded by the Swedish Research Council through grant agreement no. 2022-06725.

- **Conflicts of interest:**
The authors have no conflicts of interest to declare that are relevant to the content of this article.

- **Data availability:**
Data will be made available on request.

References

[1] J. R. Bell, D. Burton, M. Thompson, A. Herbst, J. Sheridan, Wind tunnel analysis of the slipstream and wake of a high-speed train, Journal of Wind Engineering and Industrial Aerodynamics 134 (2014) 122–138.

[2] J. R. Bell, D. Burton, M. Thompson, A. Herbst, J. Sheridan, A wind-tunnel methodology for assessing the slipstream of high-speed trains, Journal of Wind Engineering and Industrial Aerodynamics 166 (2017) 1–19.

[3] J. R. Bell, D. Burton, M. Thompson, A. Herbst, J. Sheridan, Moving model analysis of the slipstream and wake of a high-speed train, Journal of Wind Engineering and Industrial Aerodynamics 136 (2015) 127–137.

[4] L. Zhang, M. Z. Yang, J. Q. Niu, X. F. Liang, J. Zhang, Moving model tests on transient pressure and micro-pressure wave distribution induced by train passing through tunnel, Journal of Wind Engineering and Industrial Aerodynamics 191 (2019) 1–21.

[5] C. Xia, X. Shan, Z. Yang, Detached-eddy simulation of ground effect on the wake of a high-speed train, Journal of Fluids Engineering 139 (2017a).

[6] S. B. Wang, D. Burton, A. Herbst, J. Sheridan, M. C. Thompson, The effect of bogies on high-speed train slipstream and wake, Journal of Wind Engineering and Industrial Aerodynamics 83 (2018) 471–489.

[7] G. Chen, X. Li, L. Zhang, X. Liang, S. Meng, D. Zhou, Numerical analysis of the effect of train length on train aerodynamic performance, AIP Advances 12 (2022) 025201.

[8] M. Yu, R. Jiang, Q. Zhang, et al., Crosswind stability evaluation of high-speed train using different wind models, Chinese Journal of Mechanical Engineering 32 (2019) 40.

[9] S. Wordley, J. Saunders, On-road turbulence, SAE International Journal of Passenger Cars-Mechanical Systems 1 (2008) 341–360.

[10] H. Gao, T. Liu, X. Chen, H. Zeng, J. Jiang, X. Wang, B. C. Khoo, Turbulence correlation between moving trains and anemometer towers:

Theoretical analysis, field measurements and simulation, Journal of Wind Engineering and Industrial Aerodynamics 255 (2024) 105949.

[11] B. E. Lee, Some effects of turbulence scale on the mean forces on a bluff body, Journal of Wind Engineering and Industrial Aerodynamics 1 (1975) 361–370.

[12] P. W. Bearman, T. Morel, Effect of free stream turbulence on the flow around bluff bodies, Progress in Aerospace Sciences 20 (1983) 97–123.

[13] C. Zhao, H. Wang, L. Zeng, M. M. Alam, X. Zhao, Effects of oncoming flow turbulence on the near wake and forces of a 3d square cylinder, Journal of Wind Engineering and Industrial Aerodynamics 168 (2021) 177–189.

[14] M. Li, Q. Li, H. Shi, M. Li, Effects of free-stream turbulence on the near wake flow and aerodynamic forces of a square cylinder, Journal of Fluids and Structures 114 (2022) 103748.

[15] D. Burton, S. Wang, D. T. Smith, H. N. Scott, T. N. Crouch, M. C. Thompson, The influence of background turbulence on ahmed-body wake bistability, Journal of Fluid Mechanics 926 (2021).

[16] D. Schröck, N. Widdecke, J. Wiedemann, The effect of high turbulence intensities on surface pressure fluctuations and wake structures of a vehicle model, SAE International Journal of Passenger Cars-Mechanical Systems 2 (2009) 98–110.

[17] R. Hearst, G. Gomit, B. Ganapathisubramani, Effect of turbulence on the wake of a wall-mounted cube, Journal of Fluid Mechanics 804 (2016) 513–530.

[18] R. Blumrich, N. Widdecke, J. Wiedemann, A. Michelbach, F. Wittmeier, O. Beland, New fkfs technology at the full-scale aeroacoustic wind tunnel of university of stuttgart, SAE International Journal of Passenger Cars - Mechanical Systems 8 (2015) 294–305.

[19] X. Fei, T. Kuthada, A. Wagner, J. Wiedemann, The effect of unsteady incident flow on drag measurements for different vehicle geometries in an open jet wind tunnel, SAE International Journal of Advances and Current Practices in Mobility 4 (2022) 1999–2011.

[20] B. McAuliffe, A. Wall, G. Larose, Simulation of atmospheric turbulence for wind-tunnel tests on full-scale light-duty vehicles, SAE International Journal of Passenger Cars-Mechanical Systems 9 (2016a) 583–591.

[21] B. McAuliffe, A. D'Auteuil, A system for simulating road-representative atmospheric turbulence for ground vehicles in a large wind tunnel, SAE International Journal of Passenger Cars-Mechanical Systems 9 (2016b) 817–830.

[22] J. García, J. Muñoz-Paniagua, A. Jiménez, E. Migoya, A. Crespo, Numerical study of the influence of synthetic turbulent inflow conditions on the aerodynamics of a train, Journal of Fluids and Structures 56 (2015) 134–151.

[23] M. L. Shur, P. R. Spalart, M. K. Strelets, A. K. Travin, Synthetic turbulence generators for RANS-LES interfaces in zonal simulations of aerodynamic and aeroacoustic problems, Flow, Turbulence and Combustion 93 (2014) 63–92.

[24] N. Jarrin, S. Benhamadouche, D. Laurence, R. Prosser, A synthetic-eddy-method for generating inflow conditions for large-eddy simulations, International Journal of Heat and Fluid Flow 27 (2006) 585–593.

[25] D. Stoll, J. Wiedemann, Active crosswind generation and its effect on the unsteady aerodynamic vehicle properties determined in an open jet wind tunnel, SAE International Journal of Passenger Cars - Mechanical Systems 11 (2018) 429–446.

[26] X. Fei, C. Jessing, T. Kuthada, J. Wiedemann, A. Wagner, The influence of different unsteady incident flow environments on drag measurements in an open jet wind tunnel, Fluids 5 (2020) 178.

[27] D. Stoll, C. Schoenleber, F. Wittmeier, T. Kuthada, J. Wiedemann, Investigation of aerodynamic drag in turbulent flow conditions, SAE International Journal of Passenger Cars - Mechanical Systems 9 (2016) 733–742.

[28] A. P. Gaylard, N. Oettle, J. Gargoloff, B. Duncan, Evaluation of non-uniform upstream flow effects on vehicle aerodynamics, SAE International Journal of Passenger Cars-Mechanical Systems 7 (2014) 692–702.

[29] B. Duncan, L. D'Alessio, J. Gargoloff, A. Alajbegovic, Vehicle aerodynamics impact of on-road turbulence, Proceedings of the Institution of Mechanical Engineers, Part D: Journal of Automobile Engineering 231 (2017) 1148–1159.

[30] C. J. Baker, C. G. Robinson, The assessment of wind tunnel testing techniques for ground vehicles in cross winds, Journal of Wind Engineering and Industrial Aerodynamics 33 (1990) 429–438.

[31] M. Bocciolone, F. Cheli, R. Corradi, S. Muggiasca, G. Tomasini, Crosswind action on rail vehicles: Wind tunnel experimental analyses, Journal of Wind Engineering and Industrial Aerodynamics 96 (2008) 584–610.

[32] F. Cheli, S. Giappino, L. Rosa, G. Tomasini, M. Villani, Experimental study on the aerodynamic forces on railway vehicles in presence of turbulence, Journal of Wind Engineering and Industrial Aerodynamics 123 (2013) 311–316.

[33] H. Gao, T. Liu, H. Gu, Z. Jiang, X. Huo, Y. Xia, Z. Chen, Full-scale tests of unsteady aerodynamic loads and pressure distribution on fast trains in crosswinds, Measurement 186 (2021) 110152.

[34] W. Yang, H. Yue, E. Deng, Y. Wang, X. He, Y. Zou, Influence of the turbulence conditions of crosswind on the aerodynamic responses of the train when running at tunnel-bridge-tunnel, Journal of Wind Engineering and Industrial Aerodynamics 229 (2022) 105138.

[35] C. G. Robinson, C. J. Baker, The effect of atmospheric turbulence on trains, Journal of Wind Engineering and Industrial Aerodynamics 34 (1990) 251–272.

[36] J. Q. Niu, D. Zhou, X. F. Liang, Experimental research on the aerodynamic characteristics of a high-speed train under different turbulence conditions, Experimental Thermal and Fluid Science 80 (2017) 117–125.

[37] R.-D. Xue, X.-H. Xiong, X.-B. Li, G. Chen, Influence of turbulent incoming flow on aerodynamic behaviors of train at 90° yaw angle, Physics of Fluids 35 (2023) 015121.

[38] R.-D. Xue, X.-H. Xiong, G. Chen, Flow dynamics of train under turbulent inflow at different crosswind yaw angles, Physics of Fluids 36 (2024) 035176.

[39] J. García, J. Muñoz-Paniagua, A. Crespo, Numerical study of the aerodynamics of a full scale train under turbulent wind conditions, including surface roughness effects, Journal of Fluids and Structures 74 (2017) 1–18.

[40] E. Deng, H. Yue, Y.-Q. Ni, Y.-W. Wang, X.-H. He, Z.-W. Chen, A turbulent crosswind simulation method at high-speed railway tunnel entrance: Based on field test and geometric turbulence generator, Physics of Fluids 35 (2023) 015156.

[41] H. Yue, J. Wang, E. Deng, Y.-Q. Ni, W.-C. Yang, X.-Y. Liu, C.-M. Tsang, How do crosswinds from two turbulent generators affect the aerodynamic loads of running trains at tunnel entrances?, Physics of Fluids 35 (2023) 125137.

[42] W. Yang, Y. Liu, E. Deng, X. He, M. Lei, Y. Zou, Comparative study on the wind characteristics of tunnel–bridge and tunnel–flat ground infrastructures on high-speed railway, Journal of Wind Engineering and Industrial Aerodynamics 226 (2022) 105006.

[43] European Union Agency for Railways, Technical Specifications for Interoperability (TSIs), 2024. URL: www.era.europa.eu/domains/technical-specifications-interoperability_en, accessed: 2024-10-23.

[44] M. L. Shur, P. R. Spalart, M. K. Strelets, A. K. Travin, A hybrid RANS-LES approach with delayed-DES and wall-modelled LES capabilities, International Journal of Heat and Fluid Flow 29 (2008) 1638–1649.

[45] C. Xia, H. F. Wang, X. Z. Shan, Z. G. Yang, Q. L. Li, Effects of ground configurations on the slipstream and near wake of a high-speed train, Journal of Wind Engineering and Industrial Aerodynamics 168 (2017b) 177–189.

[46] Z. Zhou, C. Xia, X. Shan, Z. Yang, The impact of bogie sections on the wake dynamics of a high-speed train, Flow, Turbulence and Combustion 104 (2019) 89 – 113.

[47] J. Saunders, S. Wordley, A review of measurement of ambient turbulence with respect to ground vehicles, SAE 2006 Transactions Journal of Passenger Cars: Mechanical Systems (2006).

[48] P. L. O'Neill, D. Nicolaides, D. Honnery, J. Soria, Autocorrelation functions and the determination of integral length with reference to experimental and numerical data, in: 15th Australasian fluid mechanics conference, volume 1, University of Sydney, Sydney, NSW, Australia, 2004, pp. 1–4.

[49] E. E. Morfiadakis, G. L. Glinou, M. J. Koulouvari, The suitability of the von karman spectrum for the structure of turbulence in a complex terrain wind farm, Journal of Wind Engineering and Industrial Aerodynamics 62 (1996) 237–257.